

SIMULATIONS OF PLUME DISPERSION IN THE PASO DEL NORTE AREA

G. Wang H.J.S. Fernando E. Pardyjak N.S. Berman

(Environmental Fluid Dynamics Program, Arizona State University, Tempe, AZ 85287-9809)

Abstract

A three-dimensional time-dependent mesoscale meteorological model, HOTMAC, is applied to study the complex terrain airshed of El Paso/Ciudad Juárez. The model numerically solves the equations for mass, momentum, heat and moisture in terrain following coordinates using the alternating direction implicit (ADI) finite difference scheme. The model accounts for solar and terrestrial radiation effects, the lower boundary conditions are defined by a surface energy balance and surface layer similarity theory, and the soil heat flux is obtained by solving a 5-level heat condition equation in the soil. Surface properties are defined for 14 landuse classes and the model includes urban and forest canopy parameterizations. For the Paso del Norte region, four nested meshes (1, 2, 4 and 8 km resolution) horizontally and 22 vertical grid levels were used, with the top of the modeling domain being 6000 m. To account for synoptic-scale weather variations, a nudging scheme was employed. The numerical wind results are compared with observations made in the Paso del Norte area. Finally, using the wind and turbulence output from HOTMAC, the particle plume trajectory information was obtained using the puff dispersion model, RAPTAD, to capture in detail the pollutant motions.

INTRODUCTION

The Paso del Norte region is located along the United States – Mexico border and encompasses the cities of El Paso, Texas; Ciudad Juárez, Chihuahua; and Sunland Park, New Mexico. Air quality in this region is among the worst along the U.S. – Mexico border and this region presents a unique air pollution problem different from other urban areas in the U.S.¹ El Paso County and Sunland Park fail to meet National Ambient Air Quality Standards for PM₁₀ and ozone. El Paso County is also a non-attainment area for CO. Juárez exceeds the Mexican standards for total suspended particles, ozone and CO. The lack of rain and vegetation, frequently occurring extreme meteorological conditions, complex terrain topography, extensive unpaved urban areas, an aging and poorly maintained vehicle fleet, anthropogenic emissions from a combined population of more than two million inhabitants and other environmental factors that collude to make particulate matter (PM) a serious air pollution problem in the basin. This project was carried out in support of the Phase-II of the Paso Del Norte Air Program of the Southwest Center for Environmental Research and Policy (SCERP). First, we present simulations of the meteorology during the period of 05:00 am, Nov. 30 to 05:00 am, Dec. 3, 1998 using HOTMAC mesoscale meteorological code. The goal is to utilize both the field measurements and model simulations to better understand the

circulation patterns in the El Paso/Ciudad Juarez region. The results of a Monte-Carlo dispersion and transport model is also used to describe the migration of the pollutant plume during these days.

MODEL DESCRIPTION

HOTMAC MODEL

HOTMAC (Higher Order Turbulence Model for Atmospheric Circulations) is a three-dimensional prognostic mesoscale meteorological model utilizing a q2-1 order turbulence closure scheme.² The hydrostatic approximation, a gradient-diffusion closure scheme for the horizontal turbulence components, and a terrain-following coordinate system are used in the model.³ The effects of urban and forest canopy⁴ parameterizations (drag force, heat energy balance) are also included. A terrain-following vertical coordinate, defined by

$$z^* = \bar{H} \frac{z - z_g}{H - z_g}, \quad (1)$$

where z^* and z are the transformed and Cartesian vertical coordinates, respectively, and z_g is the ground elevation is used. Here \bar{H} is the domain depth in the terrain-following coordinate system and H is the maximum domain depth in real space. For simplicity, H is specified as

$$H = \bar{H} + z_{g \max}, \quad (2)$$

where $z_{g \max}$ is the maximum ground elevation in the computational domain. For El Paso, $z_{g \max}$ is 2796 m. Concurrent with the vertical extent of rawinsonde measurements, \bar{H} is chosen to be 6000 m. A Universal Transverse Mercator (UTM) system is used in the horizontal coordinates.

In HOTMAC, that horizontal momentum equations are written as⁵

$$\begin{aligned} \frac{D\bar{U}}{Dt} = f(\bar{V} - \bar{V}_g) + g \frac{\bar{H} - z^*}{\bar{H}} \left[1 - \frac{\langle \Theta_v \rangle}{\Theta_v} \right] \frac{\partial z_g}{\partial x} + \frac{\partial}{\partial x} \left[K_{xx} \frac{\partial \bar{U}}{\partial x} \right] + \frac{\partial}{\partial y} \left[K_{xy} \frac{\partial \bar{U}}{\partial y} \right] \\ + \frac{\bar{H}}{H - z_g} \frac{\partial}{\partial z^*} (-\overline{uw}) - \eta C_d a(z^*) \bar{U} |\bar{U}| + G_u (U_{obs} - \bar{U}), \end{aligned} \quad (3)$$

$$\frac{D\bar{V}}{Dt} = f(\bar{U} - \bar{U}_g) + g \frac{\bar{H} - z^*}{\bar{H}} \left[1 - \frac{\langle \Theta_v \rangle}{\Theta_v} \right] \frac{\partial z_g}{\partial y} + \frac{\partial}{\partial x} \left[K_{xy} \frac{\partial \bar{V}}{\partial x} \right] + \frac{\partial}{\partial y} \left[K_{yy} \frac{\partial \bar{V}}{\partial y} \right],$$

$$+ \frac{\bar{H}}{H - z_g} \frac{\partial}{\partial z^*} (-\overline{vw}) - \eta C_a a(z^*) \bar{V} |\bar{V}| + G_u (V_{obs} - \bar{V}) \quad , \quad (4)$$

where

$$\frac{D(\cdot)}{Dt} = \frac{\partial(\cdot)}{\partial t} + \bar{U} \frac{\partial(\cdot)}{\partial x} + \bar{V} \frac{\partial(\cdot)}{\partial y} + \bar{W}^* \frac{\partial(\cdot)}{\partial z^*} \quad (5)$$

The overbar denotes an ensemble average and the angle brackets for $\bar{\Theta}_v$ denote an average on the horizontal surface. The last terms in (3) and (4) represent the nudging of the modeled winds towards the observed winds, respectively. U , V and Θ_v are the X (east-west) and Y (north-south) wind components and the virtual potential temperature, respectively, \bar{W}^* is the transformed vertical velocity, \bar{U}_g and \bar{V}_g are the X and Y geostrophic wind components [$(\bar{U}_g, \bar{V}_g) = (1/f)(-\partial P/\partial y, \partial P/\partial x)$, P is the pressure], f is the Coriolis parameter, g is gravity, G_u and G_v the nudging coefficients, and U_{obs} and V_{obs} are the observations of U and V , which are obtained every twelve hours based on rawinsonde observations. The values of G_u and G_v are chosen to be $10^{-4} s^{-1}$, which is adopted from Hoke & Anthes.⁶

The continuity equation is written in the form

$$\frac{\partial \bar{U}}{\partial x} + \frac{\partial \bar{V}}{\partial y} + \frac{\partial \bar{W}^*}{\partial z^*} - \frac{1}{H - z_g} \left(\bar{U} \frac{\partial z_g}{\partial x} + \bar{V} \frac{\partial z_g}{\partial y} \right) = 0 \quad , \quad (6)$$

where

$$\bar{W}^* = \frac{\bar{H}}{H - z_g} \bar{W} + \frac{z^* - \bar{H}}{H - z_g} \left(\bar{U} \frac{\partial z_g}{\partial x} + \bar{V} \frac{\partial z_g}{\partial y} \right) \quad (7)$$

The geostrophic winds \bar{U}_g and \bar{V}_g in Eqs.(3) and (4) are computed by

$$f \bar{U}_g = f \bar{U}_g(\bar{H}) \frac{\langle \bar{\Theta}_v \rangle}{\langle \bar{\Theta}_v(\bar{H}) \rangle} + g \frac{H - z_g}{\bar{H}} \int_{z^*}^{\bar{H}} \frac{1}{\langle \bar{\Theta}_v \rangle} \frac{\partial \Delta \bar{\Theta}_v}{\partial y} dz' - \frac{g}{\bar{H}} \frac{\partial z_g}{\partial y} \int_{z^*}^{\bar{H}} \frac{\Delta \bar{\Theta}_v}{\langle \bar{\Theta}_v \rangle} dz' \quad , \quad (8)$$

$$f \bar{V}_g = f \bar{V}_g(\bar{H}) \frac{\langle \bar{\Theta}_v \rangle}{\langle \bar{\Theta}_v(\bar{H}) \rangle} + g \frac{H - z_g}{\bar{H}} \int_{z^*}^{\bar{H}} \frac{1}{\langle \bar{\Theta}_v \rangle} \frac{\partial \Delta \bar{\Theta}_v}{\partial x} dz' - \frac{g}{\bar{H}} \frac{\partial z_g}{\partial x} \int_{z^*}^{\bar{H}} \frac{\Delta \bar{\Theta}_v}{\langle \bar{\Theta}_v \rangle} dz' \quad , \quad (9)$$

where $\Delta \bar{\Theta}_v = \bar{\Theta}_v - \langle \bar{\Theta}_v \rangle$, and the abbreviated symbols $\bar{U}_g \equiv \bar{U}_g(x, y, \bar{H}, t)$, and $\bar{V}_g \equiv \bar{V}_g(x, y, \bar{H}, t)$ are used.

A simplified turbulence kinetic energy equation is given by

$$\frac{D}{Dt} \left(\frac{q^2}{2} \right) = \frac{\partial}{\partial x} \left[K_{xx} \frac{\partial}{\partial x} \left(\frac{q^2}{2} \right) \right] + \frac{\partial}{\partial y} \left[K_{yy} \frac{\partial}{\partial y} \left(\frac{q^2}{2} \right) \right] + \left(\frac{\bar{H}}{H - z_g} \right)^2 \frac{\partial}{\partial z^*} \left[q l S_q \frac{\partial}{\partial z^*} \left(\frac{q^2}{2} \right) \right] - \frac{\bar{H}}{H - z_g} \left(\overline{uw} \frac{\partial \bar{U}}{\partial z^*} + \overline{vw} \frac{\partial \bar{V}}{\partial z^*} \right) + \beta g \overline{w\theta_v} - \frac{q^3}{Bl_1} + \eta C_d a(z^*) \left[|\bar{U}|^3 + |\bar{V}|^3 \right], \quad (10)$$

where $q^2 \equiv \overline{u^2} + \overline{v^2} + \overline{w^2}$ is twice the turbulence kinetic energy, $\overline{w\theta_v}$ the turbulence heat flux, θ_v the fluctuation part of virtual potential temperature, β the thermal expansion coefficient ($=1/\langle \bar{\Theta}_v \rangle$) and $S_q, B_1 = (0.2, 16.6)$ are empirical constants.⁷ The governing conservation equations for heat and moisture are

$$\frac{D\bar{\Theta}_v}{Dt} = \frac{\partial}{\partial x} \left[K_{xx} \frac{\partial \bar{\Theta}_v}{\partial x} \right] + \frac{\partial}{\partial y} \left[K_{yy} \frac{\partial \bar{\Theta}_v}{\partial y} \right] + \frac{\bar{H}}{H - z_g} \left[\frac{\partial}{\partial z^*} (-\overline{w\theta_v}) + \frac{1}{\rho C_p} \frac{\partial R_N}{\partial z^*} \right], \quad (11)$$

$$\frac{D\bar{Q}_v}{Dt} = \frac{\partial}{\partial x} \left[K_{xx} \frac{\partial \bar{Q}_v}{\partial x} \right] + \frac{\partial}{\partial y} \left[K_{yy} \frac{\partial \bar{Q}_v}{\partial y} \right] + \frac{\bar{H}}{H - z_g} \frac{\partial}{\partial z^*} (-\overline{wq_v}), \quad (12)$$

where ρ is density, C_p is specific heat of air at constant pressure, R_N is the net radiation.

The momentum, heat and moisture fluxes are approximated using a simplified second-moment turbulence closure scheme⁸

$$\left[\overline{uw}, \overline{vw} \right] = -lq \tilde{S}_M \left[\frac{\partial \bar{U}}{\partial z}, \frac{\partial \bar{V}}{\partial z} \right], \quad (13)$$

$$\left[\overline{w\theta_v}, \overline{wq_v} \right] = -\alpha lq \tilde{S}_M \left[\frac{\partial \bar{\Theta}_v}{\partial z}, \frac{\partial \bar{Q}_v}{\partial z} \right], \quad (14)$$

where the turbulent length scale l is determined from an algebraic equation⁹

$$l = \frac{\kappa z}{1 + \kappa z / l_o}, \quad (15a)$$

$$l_o = c_1 \frac{\int_0^\infty z q dz}{\int_0^\infty q dz}, \quad c_1 = 0.1 \quad (15b)$$

κ (≈ 0.4) is the Von Karman constant, \tilde{S}_M and α are the functions of the flux Richardson number (R_f) and α ($\equiv K_H / K_M$). Here K_H ($= \alpha l q \tilde{S}_M$) is an eddy diffusivity coefficient and K_M ($= l q \tilde{S}_M$) is an eddy viscosity coefficient. The expressions for stability function, \tilde{S}_M , and α are all described in Yamada^{4,9}. The horizontal eddy viscosity coefficients K_{xx} , K_{yy} and K_{xy} are expressed as

$$K_{xx} = 2c(\Delta x)(\Delta y) \left| \frac{\partial \bar{U}}{\partial x} \right|, \quad (16a)$$

$$K_{yy} = 2c(\Delta x)(\Delta y) \left| \frac{\partial \bar{V}}{\partial x} \right|, \quad (16b)$$

$$K_{xy} = 2c(\Delta x)(\Delta y) \left\{ \left| \frac{\partial \bar{U}}{\partial x} \right| + \left| \frac{\partial \bar{V}}{\partial y} \right| \right\}, \quad (16c)$$

where $c = 0.01$. The equations are solved numerically using the alternating direction implicit (ADI) finite difference scheme. A simple 4-point diffusive smoothing scheme with smoothing parameter $\lambda = 0.3$ is used to remove $2\Delta X$ waves (see Eq. 19).

We note that the observed temperature and moisture fields are not assimilated in the integration. The reason for excluding them from the nudging procedures is that the model needs to resolve very fine variations of thermodynamic variables from the surface up to 500 m in order to produce reliable turbulence quantities. Unfortunately, the temperature and moisture measurements do not provide such a fine resolution. In other words, we prefer allowing the model to generate its own temperature and moisture variations close to the surface rather than letting the interpolated values from the observations with coarse resolution contaminate the variations.

Boundary conditions

The surface boundary conditions for (3), (4) and (10) - (12) are constructed from the empirical formulas by Dyer and Hicks¹⁰ for non-dimensional wind and temperature profiles. These formulae are valid only for horizontally homogeneous surfaces, but can be considered as fair approximations close to the surface over non-homogeneous terrain. It should be noted that land class plays an active part in the apportionment of available heat energy between convective (sensible and latent) and conductive (into soil) components. Therefore, the surface boundary conditions are defined by similarity theory and a surface energy balance between short- and long-wave energy and sensible, latent, and soil (30 cm below the surface) heat fluxes, i.e.,

$$R_N = R_s \downarrow + R_s \uparrow + R_L \downarrow + R_L \uparrow = H_s + LE + G_s \quad (17)$$

where

- R_N = net radiation
- $R_s \downarrow$ = downward shortwave radiation
- $R_s \uparrow$ = upward shortwave radiation = $R_s \downarrow (1 - \phi)$
- $R_L \downarrow$ = downward longwave radiation
- $R_{L\uparrow}$ = upward longwave radiation = $\epsilon \sigma T_G^4 + (1 - \epsilon) R_L \downarrow$
- H_s = sensible heat flux $\approx -\rho C_p u_* T_s$
- LE = latent heat flux = H_s / B
- G_s = soil heat flux = $K_s \partial T_s / \partial z_s$

ϕ the albedo, ϵ the emissivity, σ the Stefan-Boltzman constant, T_G the ground temperature, ρ the air density, C_p specific heat, u_* the friction velocity, T_s the temperature scale, B the Bowen ratio, and K_s the thermal diffusivity of the soil. The two-stream delta-eddy method is used to solve for the incoming shortwave energy flux, ¹¹ while a prescribed surface albedo determines the outgoing shortwave flux. The upward and downward longwave radiation fluxes are determined using the Stefan-Boltzman relation and the method of Sasamori, ¹² respectively. The sensible heat flux is obtained from similarity theory, while the latent heat flux is computed from a daytime-prescribed and nighttime-computed Bowen ratio. The soil heat flux is obtained by solving a 5-level heat conduction equation in the soil which ignores lateral heat transfer.

The urban and forest canopies, too small to be resolved by the mesoscale model, have been parameterized through a) the land class; b) the short- and long-wave energy flux above the ground, c) addition of an anthropogenic heating term (Q_f), d) drag in the momentum equations, and e) artificial production within the canopies. ¹³

The upper boundary (i.e., top) conditions for $\bar{U}, \bar{V}, \bar{\Theta}_v, \bar{Q}_v, q$, and l are

$$(\bar{U}, \bar{V}) = (\bar{U}_g, \bar{V}_g) \quad (18)$$

Virtual potential temperature and the mixing ratio are specified and turbulence is assumed to vanish along the upper boundary. The lateral boundary values for $\bar{U}, \bar{V}, \bar{\Theta}_v, \bar{Q}_v, q^2$ and l are obtained by integrating the corresponding governing Eqs. (3), (4), (10), (11) and (15), except that the variations in horizontal directions are all neglected. Variables \bar{U}, \bar{V}, q^2 and l are smoothed at each time step by using the values at four neighboring points, i.e.

$$\Phi_{i,j} = (1 - \lambda)\Phi_{i,j} + 0.25\lambda(\Phi_{i+1,j} + \Phi_{i-1,j} + \Phi_{i,j-1} + \Phi_{i,j+1}) \quad (19)$$

where Φ represents either $\overline{U}, \overline{V}, q^2$ or l , and $\lambda = 0.3$ is used. A similar expression, but using only three neighboring points, is applied to the values at the lateral boundaries.

Initial conditions

An initial wind profile at the southwestern corner of the computational domain is first constructed by assuming a logarithmic variation (initially $u^* = 0.2$ m/s and $z_0 = 0.1$ m) from the ground up to the level where the wind speed reaches an ambient value (geostrophic wind). Initial wind profiles at other grid locations are obtained by scaling the southwestern corner winds to satisfy the mass continuity. The vertical profile of the virtual potential temperature is initially assumed to increase linearly with height ($^{\circ}C/m$). Initial virtual potential temperatures are assumed to be uniform in the horizontal directions. Initial values for water vapor are constructed by using the initial potential temperature profiles, pressure at the top of the computational domain, and observed relative humidity. The turbulence kinetic energy and length scale are initialized by using the initial wind and temperature profiles and the relationships from the level 2 model. ¹⁴

RAPTAD MODEL

RAPTAD (Random Particle Transport And Diffusion) is a Monte-Carlo dispersion and transport code combining the attributes of random walk and puff dispersion models. ¹⁵

Pseudo-particles are transported with instantaneous velocities that include the mean wind field and turbulent velocities. The turbulent velocity is generated using the Monte-Carlo random-walk equation as ¹⁶

$$u_i(t + \Delta t) = \exp(-\Delta t / T_L) \cdot u_i(t) + \{1 - \exp(2\Delta t / T_L)\} \cdot \sigma_u \cdot \zeta \quad (20)$$

where T_L is the Lagrangian timescale, σ_u is the standard deviation of the velocity fluctuations, and ζ is a random variable chosen from a Gaussian distribution and standard deviation equal to one. The location of each pseudo-particle represents the center of the mass of a concentration distribution for each puff. The total concentration at any point is obtained by adding the concentrations of each puff at that point (a kernel method). Each puff is assumed to have a Gaussian distribution where variances are determined from the time integration of the velocity variances encountered over the history of the puff. The variances are estimated based on the random force theory of turbulent diffusion. Plume-rise is computed using the Briggs formulae. ¹⁷

NUMERICAL PROCEDURE

The simulations were performed on a 4-nested mesh horizontally encompassing the El Paso area. ¹⁸ The horizontal mesh system is given in Table 1. Since winds, temperatures, and water vapor are known to vary greatly with height near the surface, the vertical grid levels are chosen to vary linearly with the height near the ground with a grid interval of 5 m in terrain-following coordinates for the lowest five cells; the grid size parabolically

extends at greater heights. The height of computational box is to 6000 m (Table 2). The vertical grid size varied as $z_s = 0.0$ to 0.303 m (Table 3) for soil layers.

Table 1: Horizontal grid parameters

Mesh type	SW corner (utm, km)	NE corner (utm, km)	Grid size (km)	No. of grids E-W dir.	No. of grids N-S dir
coarser	228; 3228	484; 3756	8	32	66
coarse	300; 3460	420; 3580	4	30	30
medium	320; 3480	400; 3560	2	40	40
fine	336; 3490	376; 3540	1	40	50

Table 2: Vertical mesh coordinates (atmosphere)

Level (No.)	Grid level (m) ($\bar{U}, \bar{V}, \bar{\Theta}, \bar{Q}$)	Half-grid level (m) (\bar{W}^*, q^2, K_M, K_H)
1	0.0	0.0
2	5.0	2.5
3	10.0	7.5
4	15.0	12.5
5	20.0	17.5
6	25.0	22.5
7	53.0	33.3
8	127.1	84.3
9	247.2	181.4
10	413.4	324.6
11	625.7	513.6
12	884.0	749.1
13	1188.3	1030.4
14	1538.8	1357.8
15	1935.2	1731.2
16	2377.7	2150.7
17	2866.3	2616.3
18	3400.9	3127.9
19	3981.6	3685.5
20	4608.4	4289.2
21	5281.2	4939.0
22	6000.0	5634.8

Table 3: : Vertical mesh coordinates (soil)

Level (No.)	Grid level (m) ($\bar{U}, \bar{V}, \bar{\Theta}, \bar{Q}$)	Half-grid level (m) (\bar{W}^*, q^2, K_M, K_H)
1	0.0	0.0
2	0.009	0.003
3	0.054	0.024
4	0.159	0.1

5	0.303	0.228
---	-------	-------

Figure 1 shows the outermost terrain of El Paso area. The Rio Grande separates El Paso to the north from Ciudad Juarez to the south. El Paso wraps around the southern tip of the Franklin Mountains, while Ciudad Juarez extends westward onto the foothills of the Sierra Juarez and spreads south-southeast following the Rio Grande. The topography used for these simulations was obtained from the USGS 3-second U.S. and 30-second global DEM datasets.

Surface properties are defined for 14 landuse classes and the model includes urban and forest canopy parameterizations. Figure 2 (a), (b), (c) and (d) shows the landuse map of the 4-nested grid system. The urban areas are surrounded by desert scrubland, except for irrigated regions along the Rio Grande. Landuse for the U.S. side of the border was derived from USGS LULC dataset while landuse on the Mexican side on the border was obtained from a combination of 1:100,000 and 1:50,000 scale topographical maps. The landuse is known to have been last updated with 1970's aerial photographs, and hence we expect that our estimated urban coverage to be underestimated.

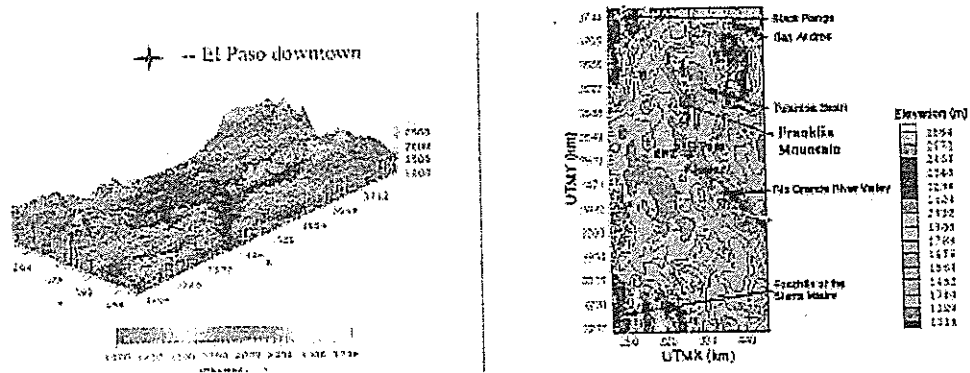
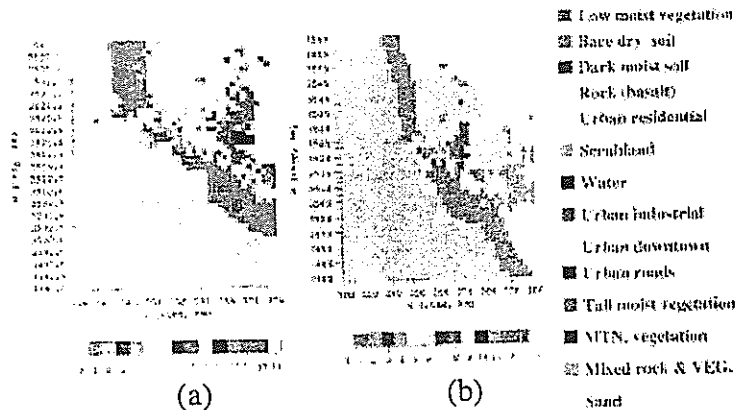


Figure 1 Surface topography used in the HOTMAC outermost grid mesh (8 km resolution)



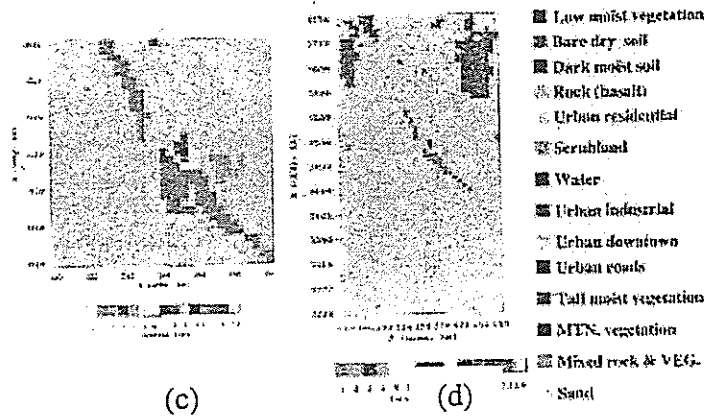


Fig. 2: Land use map for 4-nest grid resolutions: (a) 1 km (b) 2 km (c) 4 km (d) 8 km

RESULTS AND DISCUSSIONS

The meteorological simulations began at 17:00 LST on Nov. 29 (Julian day=333), 1998 and lasted roughly eighty-four hours. The initial conditions for the simulations were obtained from a Santa Teresa (EPZ site, UTMX=339.238 km, UTM Y=3530.425) rawinsonde sounding. Horizontal homogeneity was imposed on the initial meteorological fields since we are using only one vertical profile; hence, some spin-up time is needed to allow the model to overcome the over-simplified starting conditions. In this paper, the first twelve hours of the model simulation are not used to allow for the model spin-up.

In order to capture the upper-level jet and changing synoptic conditions, a data assimilation scheme using the EPZ rawinsonde wind profiler data taken at 12 hour intervals was used to 'nudge' the winds. The nudging radius-of-influence linearly increased from 2 km at the ground to 400 km at the domain top; however, nudging was turned off below 500 meters agl to allow the development of locally driven thermal flows.

Figure 3 (a), (b) shows the initial conditions used in HOTMAC of virtual potential temperature and relative humidity respectively from the experimental data.

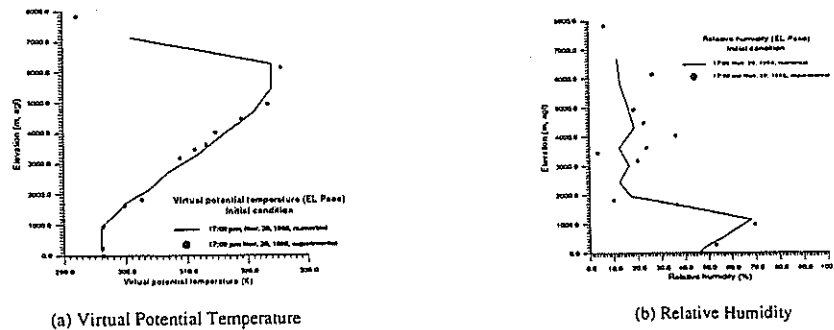


Figure 3: Initial conditions setup from experimental data: (a) Virtual potential temperature; (b) Relative humidity; Solid line (-): Numerical; Dot (•): Experimental

Wind Data Comparisons

In this section, the computed results for the vertical profiles of wind speed and wind direction are compared with the EPZ field data (Figure 4 – 8). Figure 4 (a), (b) shows wind speed and wind direction in the morning before sunrise (05:00 LST) on Nov. 30, 1998. The computed results predict a low level jet that is absent from the EPZ site data.

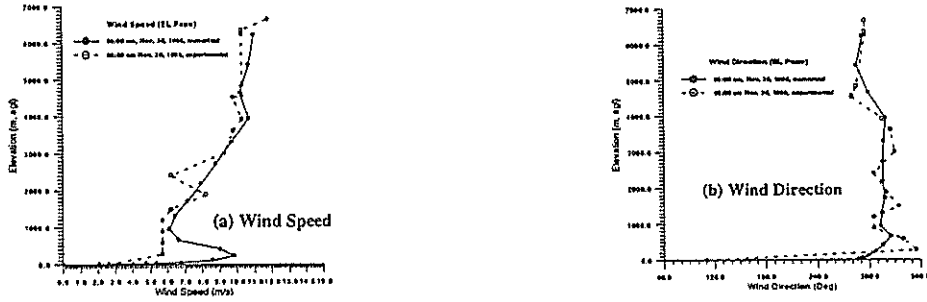


Figure 4: Wind results comparison between model-produced and experimental in EPZ site on 05:00 LST of Nov. 30, 1998: (a) wind speed; (b) wind direction; Dot (•): Numerical; Circle (◦): Experimental

Figure 5 (a), (b) shows another early morning low level jet predicted for Dec. 1, 1998 (05:00 LST), which is in general agreement with the observations. The depth and magnitude of the jet are fairly well described by HOTMAC, but the direction of the jet is incorrect. This indicates that the mechanism of the jet formation or the topographic source responsible for the jet is not correctly captured by the model. A similar conclusion can be inferred by the 05:00 LST prediction of Dec. 3 (see Figure 7 below).

Figure 6 and 8 show that the afternoon (1700 LST) lower winds are better predicted than the in the morning cases. In all cases, as expected, the ‘nudging’ scheme produces better agreement with the experimental data at the higher altitudes. The discrepancies near the surface may be due to combination of the poor resolution of the local topography, oversimplified parameterizations of the surface terrain, and the large difference in land-use between the out-dated DEM data and the actual city at the time of measurement.

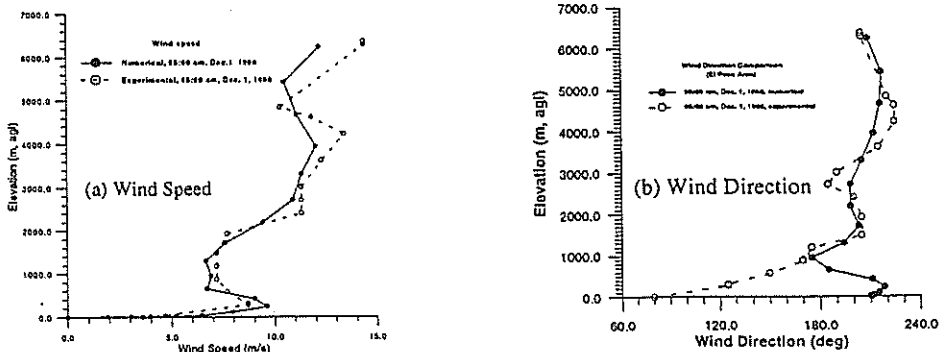


Figure 5: Comparison between model-produced and experimentally observed winds at the EPZ site on 05:00 LST of Dec. 1, 1998: (a) wind speed; (b) wind direction; Dot (●): Numerical; Circle (○): Experimental.

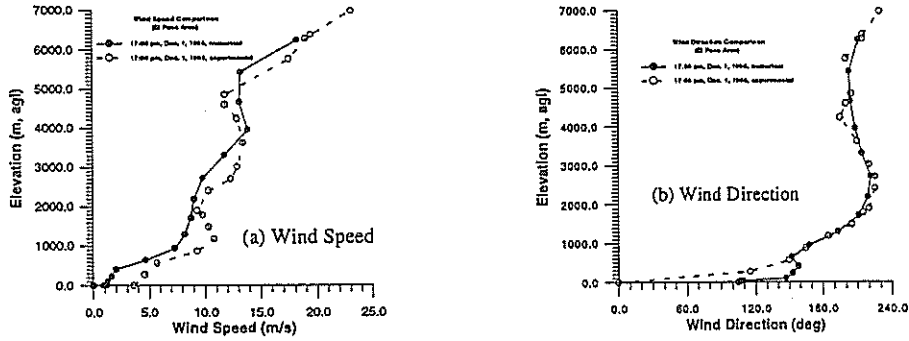


Figure 6: Comparison between model-produced and experimentally observed winds at the EPZ site on 1700 LST of Dec: 1, 1998: (a) wind speed; (b) wind direction; Dot (●): Numerical; Circle (○): Experimental

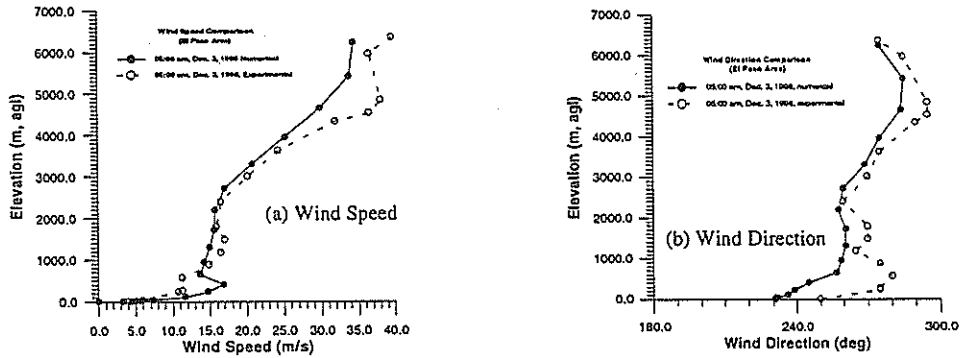


Figure 7: Comparison between model-produced and experimentally observed at the EPZ site on 0500 LST of Dec. 3, 1998: (a) wind speed; (b) wind direction; Dot (●): Numerical; Circle (○): Experimental

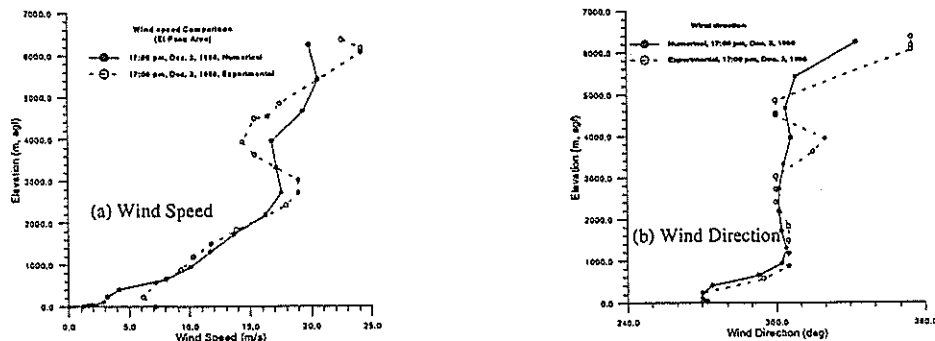


Figure 8: Comparison between model-produced and experimental in EPZ site on 1700 LST of Dec. 3, 1998: (a) wind speed; (b) wind direction; Dot (•): Numerical; Circle (◦): Experimental

Prediction of Plume Trajectories

The figures given below represent the plume trajectories calculated by the RAPTAD schme, based on the wind and turbulence results from HOTMAC and the horizontal velocity distribution at 10 m above the ground level at corresponding time intervals. We assume that the source located at UTMX= 328 km, UTMY= 3520 km, height= 1256.0 msl which is quite near to the border, to begin releasing particles at 1600 LST of Nov. 30, 1998. Figure 9 shows the change of the upper-layer wind direction with time at he EPZ site.

Figures 10-16 show instantaneous snapshots of the horizontal velocity vector field taken at 10 m above the ground level at several time increments starting from 1700 LST on November 30, 1998. Accompanying these vector data are the 3D plume trajectory plots. Both figures have data plotted on the calculation domain's topography. As described above, the plume trajectories were obtained using RAPTAD. Wind and turbulence data were obtained from HOTMAC and used as input for RAPTAD.

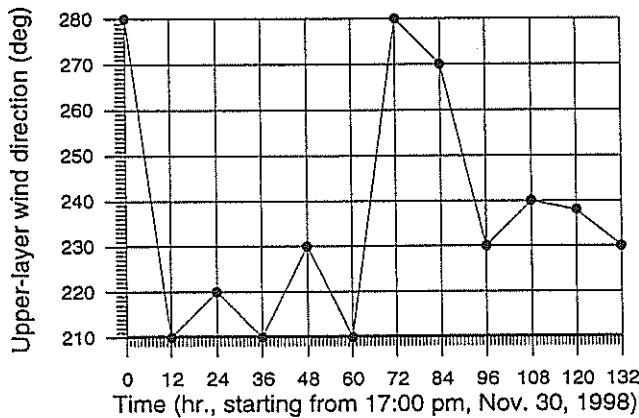


Figure 9: Upper-layer wind direction changing with time in EPZ site

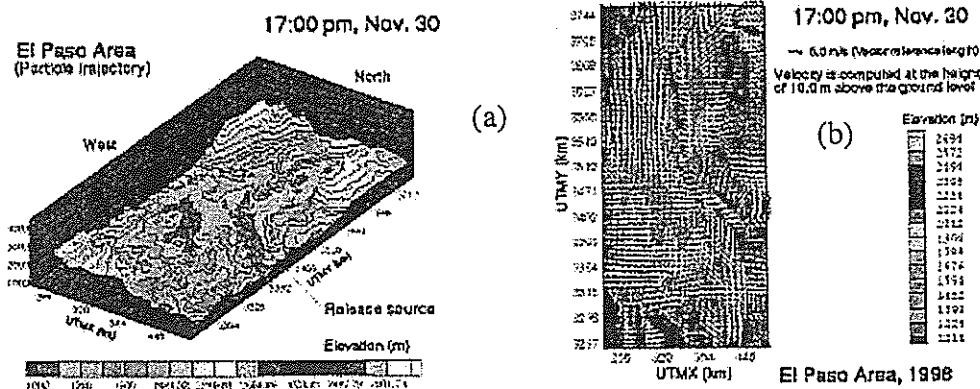


Figure 10: 3-D plume trajectory and velocity distribution at 1700 LST on Nov. 30, 1998. (a) plume; (b) velocity at 10 m, agl. Elapsed time: 1 hour, upper wind = 277° .

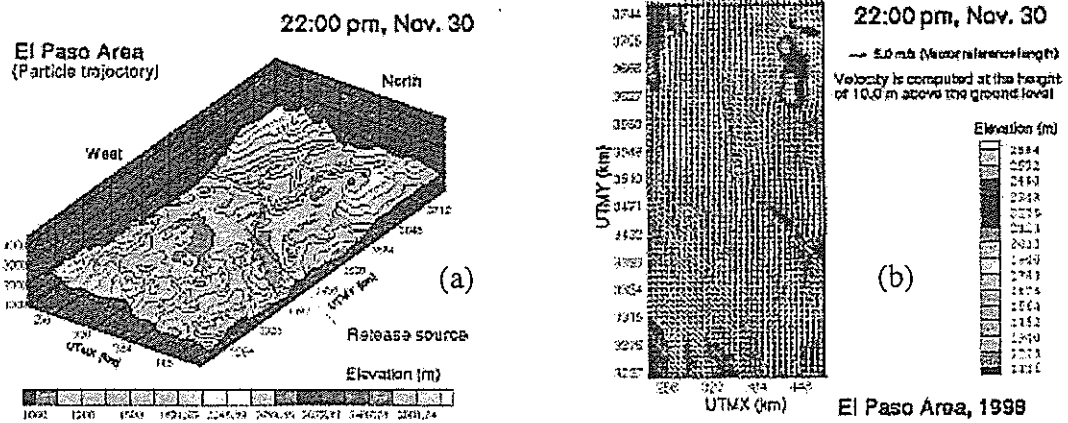


Figure 11: 3-D plume trajectory and velocity distribution at 2200 LST on Nov. 30, 1998. (a) plume; (b) velocity at 10 m, agl. Elapsed time: 6 hours, upper wind = 246° .

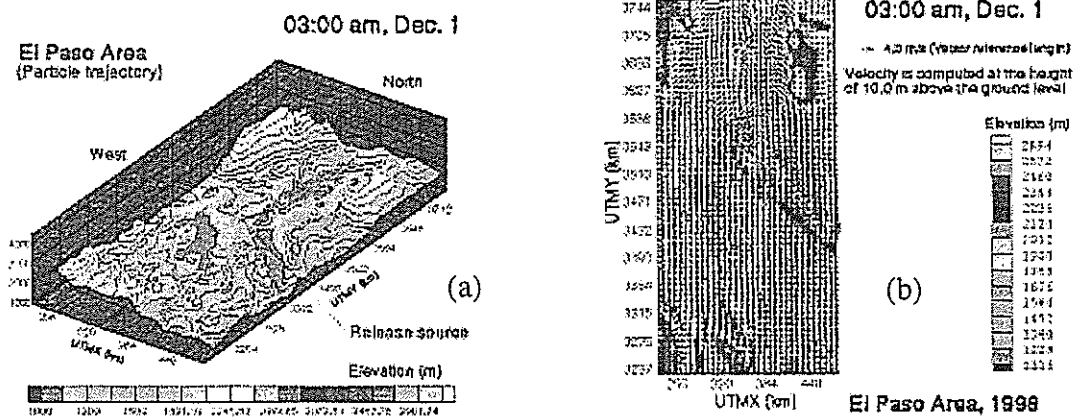


Figure 12: 3-D plume trajectory and velocity distribution at 0300 LST on Dec. 1, 1998. (a) plume; (b) velocity at 10 m, agl. Elapsed time: 11 hours, upper wind = 216° .

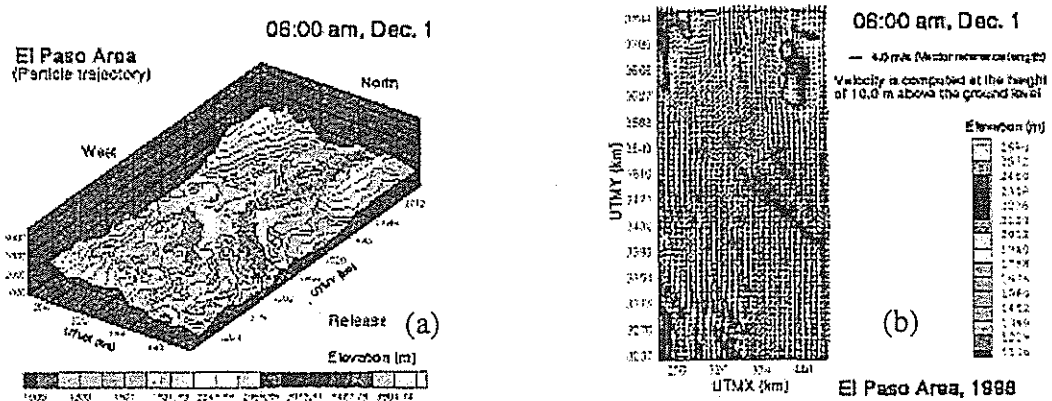


Figure 13: 3-D plume trajectory and velocity distribution at 0600 LST on Dec. 1, 1998. (a) plume; (b) velocity at 10 m, agl. Elapsed time: 14 hours, upper wind = 211° .

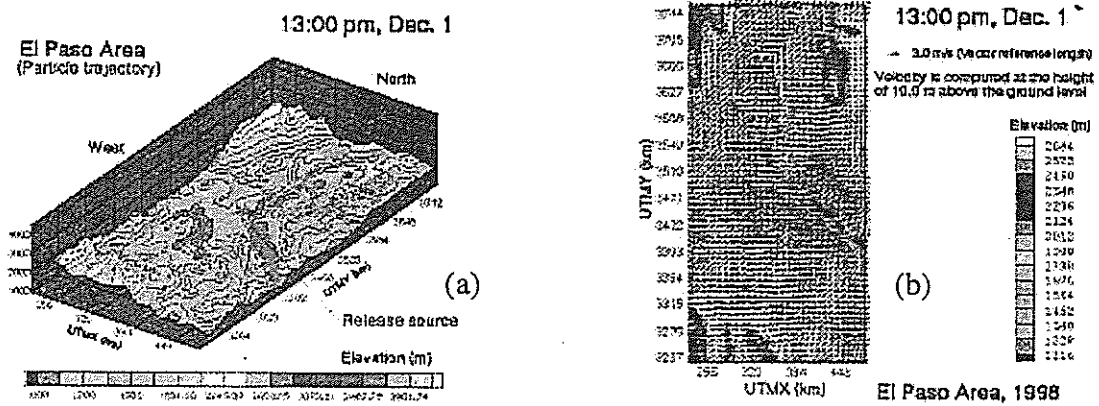


Figure 14: 3-D plume trajectory and velocity distribution at 1300 LST on Dec. 1, 1998. (a) plume; (b) velocity at 10 m, agl. Elapsed time: 21 hours, upper wind = 217° .

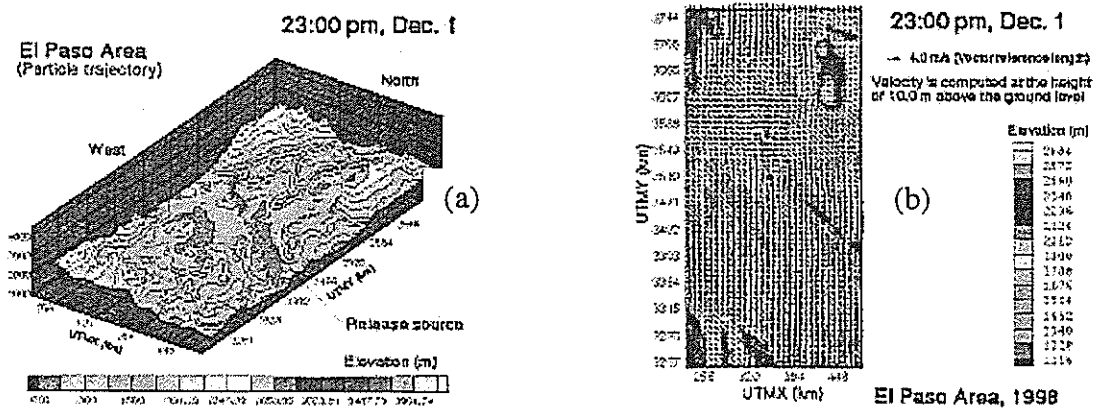


Figure 15: 3-D plume trajectory and velocity distribution at 2300 LST on Dec. 1, 1998. (a) plume; (b) velocity at 10 m, agl. Elapsed time: 31 hours, upper wind = 214° .

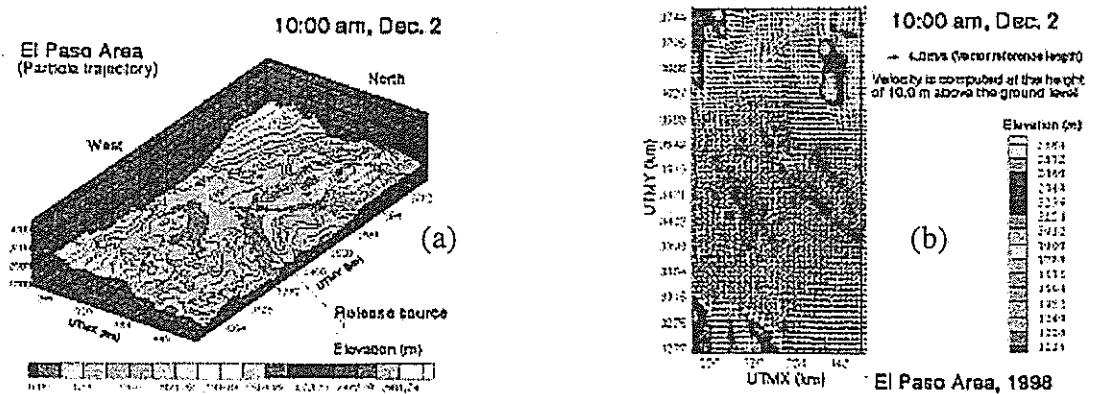


Figure 16: 3-D plume trajectory and velocity distribution at 1000 LST on Dec. 2, 1998. (a) plume; (b) velocity at 10 m, agl. Elapsed time: 42 hours, upper wind = 220° .

Figures 10(a) and 11(a) show the north-easterly motion of the plume toward Franklin Mountain, following the near-surface flow driven by the upper level winds. Due to the stable conditions, the plume moved around the west side of the mountain. It was then diverted south-westward by the down-valley winds from the north-west and proceeded towards San Andres Mountain. The prevailing wind continued to push the plume northward as the slope winds from San Andres Mountain forced the flow to stay in the valley.

As shown in Figure 14(a), by 1300 LST, thermal convection dominated the flow during the mid-day and the plume was vertically mixed and carried away by the upper level winds. By 2300 LST, the plume had moved toward the north-west by an up-valley flow (Figure 15(a)) until it reached an altitude where it was scrubbed away by the synoptic flow toward San Andres Mountain.

Finally, Figure 16(a) shows the plume at 1000 LST on Dec. 2, 1998. The plume was directed north-eastward by the up-valley and prevailing winds. The figure shows little dispersion of the plume until it reached San Andres Mountain where it appears to be mixed by late morning convection.

As shown in Figure 9, the upper level winds were predominately from the west and south-east. This was evident in the plumes as a northward motion that was diverted periodically by the local thermally driven flow.

Conclusions

HOTAMC mesoscale meteorological model was used to calculate air flow and dispersion in the El Paso-Juarez area. Near the ground, the model-produced wind speed profiles showed a reasonable agreement with rawinsonde measurements although wind direction was not correctly predicted at nighttimes. The RAPTAD Lagrangian dispersion model was used to study the plume dispersion in this area based on wind vector predictions of HOTMAC. The advection of the plume in the developing boundary layer, its impingement on the terrain, entrainment in the upper-layer wind and dispersion by thermal convection were observed to be the major features of the flow.

Acknowledgements

We wish to thank Dr. Michael Brown for his generous guidance and critical comments during this work. This work was funded in part by the Southwest Center for Environmental Research and Policy (SCERP) and the office of Vice President for Research at ASU. We also wish to acknowledge the support of Prof. David Pijawka in carrying out this study.

References

1. Roberts et. al., 1996: Summary of measurements obtained during the 1996 Paso Del Norte Ozone Study, STI-996191-1603-FR.

2. T. Yamada, T. and S. Bunker, 1989: A numerical model study of nocturnal drainage flows with strong wind and temperature gradients, *J. Appl. Meteor.*, 28, pp. 545-554.
3. M. Williams, and T. Yamada et. al., 1989: The Los Alamos National Laboratory Atmospheric Transport and Diffusion Models: User Manual.
4. T. Yamada, 1982: Simulations of nocturnal drainage flows by a q^2 turbulence closure model, *J. Atmos. Sci.*, Vol. 40, pp. 91-106.
5. T. Yamada, 1981: A numerical model study of turbulent airflow in and above a forest canopy, *J. of the Meteorological Society of Japan*, Vol. 60, No. 1, pp. 439-454.
6. Hoke, J. E., and R. A. Anthes, 1977: Dynamic initialization of a three-dimensional primitive-equation model of Hurricane Alma of 1982, *Mon. Wea. Rev.* 105, pp. 1266-1280.
7. G. L. Mellor, T. Yamada, 1982: Development of a turbulence closure model for geophysical fluid problems, *Rev. Geophys. Space Phys.* Vol. 20(4), pp. 851-875.
8. T. Yamada, 1983: Simulations of Nocturnal Drainage Flows by a q^2 Turbulence Closure Model, *J. Atmos. Sci.*, 40, 91-106.
9. G. L. Mellor, T. Yamada, 1974: A hierarchy of turbulence-closure models for planetary boundary layer, *J. Atmos. Sci.*, 31, 1791-1806.
10. Dyer, A. J. and B. B. Hicks, 1970: Flux-Gradient relationships in the constant flux layer, *Quart. J. Roy. Meteor. Soc.*, 96, 715-721.
11. W. Smith, and C. Kao, 1996: Numerical simulations of observed arctic stratus clouds using a second-order turbulence closure model, *J. Appl. Meteor.*, Vol. 35, pp. 47-59.
12. T. Sasamori, 1968: The radiative cooling calculation for application to general circulation experiments, *J. Appl. Meteor.*, Vol. 7, pp. 721-729.
13. Michael J. Brown, and Michael D. Williams, 1997: The effect of urban canopy parameterizations of mesoscale meteorological model simulations in the Paso Del Norte Area, submitted to: Air and Waste Management Association's 90th Annual Meeting, June 8-13, Toronto, Canada.
14. T. Yamada, and G. L. Mellor, 1975: A simulation of the Wangara atmospheric boundary layer data, *J. Atmos. Sci.*, Vol. 32, pp. 2309-2329.
15. M. Williams, and T. Yamada, 1990: A microcomputer-based forecasting model: potential applications for emergency response plans and air quality studies, *J. Air Waste Manage. Assoc.*, Vol. 40, pp. 1266-1274.
16. Michael J. Brown, and Michael D. Williams, 1996: Plume dispersion sensitivity to upper-level wind variations in a Chilean coastal environment, submitted to: Air & Waste Waste Management Association 89th Annual Meeting and Exhibition.
17. G. Briggs, 1984: Plume rise and buoyancy effects, *Atmospheric Science and Power Production* (ed. D. Randerson), U.S. Dept. of Energy, DOE/TIC-27601, pp. 327-366.
18. Michael J. Brown, Keeley Costigan, Cathrin Muller and G. Wang, 1999: Meteorological simulations of Ozone Episode Case Days During the 1996 Paso Del Norte Area, submitted to: Air and Waste Management Association's 92th Annual Meeting, August, St. Louis, USA.

Key words

mesoscale meteorological model, finite different method, Paso del Norte Ozone Study, hydrostatic approximation, terrain-following coordinate system, ADI, nested grid, nudging scheme, complex terrain